Atmospheric
Measurement
Techniques

Lidar arc scan uncertainty reduction through scanning geometry optimization

Hui Wang[1], Rebecca J. Barthelmie[1], Sara C. Pryor[2], and Gareth. Brown[3]

[1]Sibley School of Mechanical and Aerospace Engineering, Cornell University, Ithaca, New York, USA
[2]Department of Earth and Atmospheric Sciences, Cornell University, Ithaca, New York, USA
[3]SgurrEnergy Ltd, Vancouver, British Columbia, Canada

Correspondence to: Hui Wang (hw524@cornell.edu)

Abstract. Doppler lidars are frequently operated in a mode referred to as arc scans, wherein the lidar beam scans across a sector with a fixed elevation angle and the resulting measurements are used to derive an estimate of the *n* minute horizontal mean wind velocity (speed and direction). Previous studies have shown that the uncertainty in the measured wind speed originates from turbulent wind fluctuations and depends on the scan geometry (the arc span and the arc orientation). This paper is designed to provide guidance on optimal scan geometries for two key applications in the wind energy industry: wind turbine power performance analysis and annual energy production prediction. We present a quantitative analysis of the retrieved wind speed uncertainty derived using a theoretical model with the assumption of isotropic and frozen turbulence, and observations from three sites that are onshore with flat terrain, onshore with complex terrain and offshore, respectively. The results from both the theoretical model and observations show that the uncertainty is scaled with the turbulence intensity such that the relative standard error on the 10 min mean wind speed is about 30 % of the turbulence intensity. The uncertainty in both retrieved wind speeds and derived wind energy production estimates can be reduced by aligning lidar beams with the dominant wind direction, increasing the arc span and lowering the number of beams per arc scan. Large arc spans should be used at sites with high turbulence intensity and/or large wind direction variation.

1 Introduction

Coherent Doppler lidars (hereafter called lidars) have been used to probe a range of atmospheric boundary layer (ABL) phenomena, including nocturnal low level jets in the Great Plains (Banta et al., 2008), spatial variability of wind in the marine ABL (Pichugina et al., 2012), structures of the urban ABL (Calhoun et al., 2006; Frehlich et al., 2006) and turbulent properties and flow patterns over complex terrain (Krishnamurthy et al., 2011; Choukulkar et al., 2012). Lidars also have applications in wind energy resource estimation and wake characterization (Banta et al., 2013; Barthelmie et al., 2013) due to their ability to accurately and precisely measure flow structures both in front of and in the wake of a wind turbine (Simley et al., 2013; Aitken et al., 2014) and spatial variability of wind speeds over prospective wind farms (Krishnamurthy et al., 2013).

Lidar measurements usually involve operating the instrument with a scan geometry to acquire radial velocities from at least three directions and estimating wind velocity according to the following equation:

$$v_r(s) = \boldsymbol{d}^T \boldsymbol{u}, \tag{1}$$

where $\boldsymbol{d}^T = [\cos\phi\sin\theta, \cos\phi\cos\theta, \sin\phi]$ and $\boldsymbol{u}^T = [u, v, w,]$. The radial velocity v_r is the projection of the wind velocity $\boldsymbol{u}$ on the line of sight (LOS) at the location $\boldsymbol{s} = s\boldsymbol{d}$ for which s is the distance from the lidar along the LOS and $\boldsymbol{d}$ is the unit directional vector determined by the elevation angle ϕ and the azimuth angle θ of the LOS from north. The uncertainty or standard error of the estimated wind velocity has great importance to wind energy applications

and is a function of the atmospheric turbulence structure and the specific lidar scanning geometry (Banakh et al., 1995). Two common scanning geometries applied in wind energy are the velocity-azimuth-display (VAD) scan and the arc scan. VAD scans apply a full-azimuth conical scan (i.e., θ from 0 to 360°) with a constant elevation angle (ϕ) and the wind velocity is estimated by solving Eq. (1) under the assumption of a horizontally homogeneous wind field. When the assumption is met VAD scans are reliable and well understood and can meet the stringent accuracy requirement for wind energy applications (Gottschall et al., 2012). The arc scan involves ϕ being held constant and θ varied to sample a conical sector (e.g., Henke and Clive, 2015). VAD scans are commonly used for wind resource assessment because in homogeneous terrain or under a constant wind gradient the function used to derive the wind velocity should have the smallest errors, while arc scans can potentially have large errors if the fit is distorted by a small number of erroneous points. However, arc scans "are less affected by inhomogeneities in the wind field on scales of the scan diameter than are the full circle scans" (Schwiesow et al., 1985). Arc scans have a role, especially if heterogeneous conditions exist, because the scan can be focused on the region of interest. For example, a VAD scan centered at the hub of an operating wind turbine will be affected by inhomogeneity because of the wind turbine wake. If the purpose of measurement is the freestream wind speed, a smaller sector scan or arc scan upwind of the wind turbine can be more suitable than a full conical scan. Arc scans also have the advantage that by only sampling the area of interest, the number of sample repetitions in a given time can be increased, decreasing the statistical uncertainty in solving Eq. (1). Use of arc scans adds two additional parameters to the scanning geometry: (1) the arc span (i.e., the width of the scan sector, $\Delta\theta$) and (2) the angle between the center of the arc and the wind direction, which is a measure of the orientation of the arc scan and will be called hereafter the relative direction and denoted as β. The selection of these parameters have implications for the accuracy of the retrieved wind speed (Courtney et al., 2014; Wang et al., 2015). Here we extend prior work on optimizing scan geometry to minimize the uncertainty in the estimated wind speeds. We present a quantitative analysis of the dependence of the retrieved wind speed uncertainty on scanning geometry and turbulence intensity, and provide a tool for use in planning lidar deployments for wind energy applications such as power performance tests. The analysis uses both a theoretical turbulence model and real arc scan measurements from a pulsed lidar deployed in three different geographic locations characterized by different surface roughness and turbulence regimes. We conclude by demonstrating how the wind speed uncertainty from lidar arc scan measurement is propagated to the uncertainty in predicting annual energy production (AEP).

Table 1. Galion G4000 Doppler wind lidar specification[1].

Parameter	Value
Wave length	1.56 μm
Pulse energy	30 μJ
Pulse duration[2]	200 ns (30 m)
Range gate size	30 m
Spatial Resolution[3]	60 m
Aperture diameter	75 mm
Pulse repetition frequency	20 kHz
Sampling frequency	100 MHz
Dwell time	1 s
Radial velocity accuracy	0.1 m s^{-1}

[1] This specification is provided by SgurrEnergy. [2] Full width at half maximum. [3] Spatial resolution is the sum of the pulse duration and the range gate size (Frehlich, 1997).

2 Uncertainty in the lidar radial velocity

Uncertainties in measured radial velocities from a pulsed lidar (e.g., Sgurr's Galion lidar from which measurements are presented herein, Table 1) are well characterized (Frehlich and Yadlowsky, 1994; Frehlich, 1997) and can be described as follows:

$$v_R = v_{R0} + e + \delta, \tag{2}$$

where v_R is the measured radial velocity, v_{R0} is the true radial velocity in the sensing volume, δ is the bias due to systematic errors and e is the random error which has zero mean and variance σ_e^2. The magnitude of σ_e^2 is a function of both the signal-to-noise ratio (SNR) and the radial velocity variance ($\sigma_{v_r}^2$) in the sensing volume. The true radial velocity from a range gate is well approximated by the weighted average of radial velocities in the sensing volume as (Frehlich, 1997):

$$v_{R0}(r) = \int_0^\infty v_r(s) W(r-s) \mathrm{d}s, \tag{3}$$

where r is the lidar range gate location on the LOS, and $W(r-s)$ is a weighting function with its peak value at $s = r$. Note that we use v_r to denote a radial velocity at a point location and v_R a measured (volumetrically averaged) radial velocity.

The precision of v_R is bounded by the Cramer–Rao Bound (CRB) which is a function of SNR (Pearson and Collier, 1999). The relationship between CRB and SNR derived from Eq. (5) in Pearson and Collier (1999), and that estimated from radial velocity measurements using the autocorrelation method from Frehlich (2001) are shown in Fig. 1 for the Galion lidar. Both show that CRB decreases exponentially with increasing SNR, and for the Galion lidar, σ_e^2 has the lower bound of 0.01 m^2 s^{-2} when SNR > -20 dB.

The uncertainty in v_R scales with turbulence intensity due to fluctuations of both wind speed and backscattering parti-
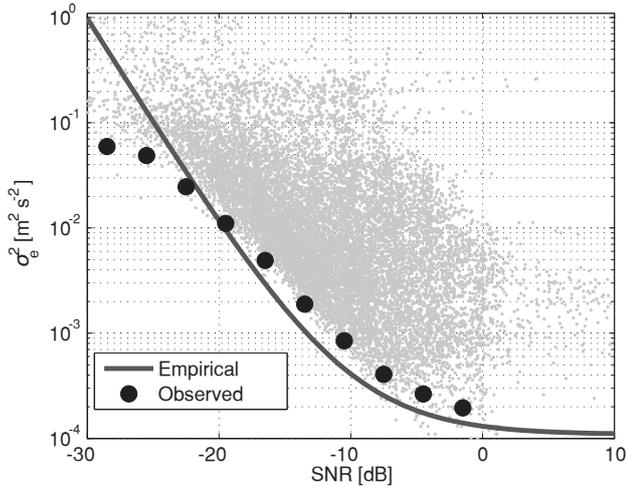
Figure 1. The relationship between the signal-to-noise ratio (SNR) and the radial velocity random error variance (σ_e^2). The gray dots show the observed radial velocity variance approximated by the difference between the variance and the autocovariance at one time lag of the radial velocities collected in an experiment in which the lidar was operated with a staring mode at the US National Renewable Energy Laboratory (Wang et al., 2015), and the observed Cramer–Rao Bound (CRB) (filled dark circles) is approximated by the mean of the lowest 5 % of the gray dots (Frehlich, 2001). The empirical relationship between the SNR and the CRB is denoted by the dark solid line and is based on Eq. (5) in Pearson and Collier (1999).

cle locations in the sensing volume can broaden the signal spectrum and thus increase the uncertainty in v_R (Banakh et al., 1995; Frehlich, 1997). When the turbulence is sufficiently strong ($\sigma_{v_r} \geq 0.5 w_R$ where w_R is the spectrum width of lidar signal in velocity space that is $\sim 0.877\,\mathrm{m\,s^{-1}}$ for the Galion lidar), the random error variance σ_e^2 becomes proportional to σ_{v_r}. If σ_{v_r} is extremely large, the spectrum width will be such that the peak is indistinguishable from the noise and thus the radial velocity selected by an estimator can be any value within the velocity search space ($\pm 39\,\mathrm{m\,s^{-1}}$ for the Galion lidar).

Other sources of error in v_R include non-linear vertical wind shear which can introduce a bias in radial velocity measurement (Lindelöw et al., 2008), and lidar misalignment which results in incorrect azimuth and elevation angles so the measured radial velocity does not represent the wind field at the intended location. For a well-secured ground-based lidar pitch (displacement from the horizontal) and roll (i.e., "tilt") angles can be measured and are usually much lower than 1°, causing negligible errors.

The synthesis given above thus indicates that when SNR is reasonably high, the uncertainty in v_R is small ($\sigma_e^2 < 0.01\,\mathrm{m^2\,s^{-1}}$), and makes a much smaller contribution to the overall uncertainty in the derived horizontal wind speed than turbulent wind fluctuations in the sampling volume (as shown in the next section). Hence, the uncertainty in v_R will not be

considered further in calculating the uncertainty in the estimated mean wind speed from arc scans.

3 Uncertainty in wind speeds derived from lidar arc scan measurements

As in other Eulerian measurement systems (e.g., a network of anemometers deployed on meteorological masts), a lidar conducting arc scans measures the wind velocity by sampling the wind field with a specified sampling frequency and spatial coverage, but the lidar only measures the radial velocity, and wind velocity needs to be estimated using an inverse method applied under certain assumptions about the wind field. When the radial velocity has negligible errors, the uncertainty in the estimated wind velocity is controlled by (1) the spatial statistics of the wind field that determine the variation of and the correlation between the samples (and hence effective sample size, and the representativeness of the wind field), (2) the scanning geometry that determines the temporal and spatial resolution of the samples and (3) the stability of the inverse method. In this section, we describe how the uncertainty in the estimated mean horizontal wind speed from arc scans (denoted as V_l) is related to the characteristics of the wind field and the scanning geometry. The method used follows that of Banakh et al. (1995) which was developed to evaluate the uncertainty of wind velocities estimated from VAD scans.

In a homogeneous and stationary wind field, the covariance between the ith and jth radial velocities, which are measured by a lidar at the range gates centered at $\boldsymbol{r}_i = r_i \boldsymbol{d}$ and $\boldsymbol{r}_j = r_j \boldsymbol{d}$, respectively, is a function of the relative location between these two measurements. With the assumption of frozen turbulence, the relative location between the two measurements is $\boldsymbol{p}_{ij} = \boldsymbol{r}_i - \boldsymbol{r}_j - \Delta \boldsymbol{p}_{ij}$ where $\Delta \boldsymbol{p}_{ij} = [(i - j)\delta t]\boldsymbol{u}_0$ is the separation distance induced by the mean wind velocity $\boldsymbol{u}_0 = (u_0, v_0, w_0)$ during a time interval $(i - j)\delta t$. The covariance between the two radial velocity measurements (a_{ij}) then can be written as follows:

$$a_{ij}(\boldsymbol{p}_{ij}) = \int\!\!\int\limits_0^\infty [W(s_i - r_i)W(s_j - r_j)K_r(\boldsymbol{q}_{ij})]\mathrm{d}s_i\mathrm{d}s_j, \quad (4)$$

where $\boldsymbol{q}_{ij} = \boldsymbol{s}_i - \boldsymbol{s}_j - \Delta \boldsymbol{p}_{ij}$. The term $K_r(\boldsymbol{q}_{ij})$ is the covariance between the point radial velocities (v_r) separated by $\boldsymbol{q}_{ij}$ that is related to the covariance matrix $\mathbf{C}(\boldsymbol{q}_{ij})$ of wind velocities with the same separation distance:

$$K_r(\boldsymbol{q}_{ij}) = \boldsymbol{d}_i^T \mathbf{C}(\boldsymbol{q}_{ij})\boldsymbol{d}_j. \quad (5)$$

The entries in the covariance matrix $\mathbf{C}$ are the ensemble variance and covariance between three orthogonal wind components. Note no summation is assumed over repeated indices in Eqs. (4) and (5). Let $\mathbf{A}$ denote the covariance matrix for all measured radial velocities within a 10 min period. The
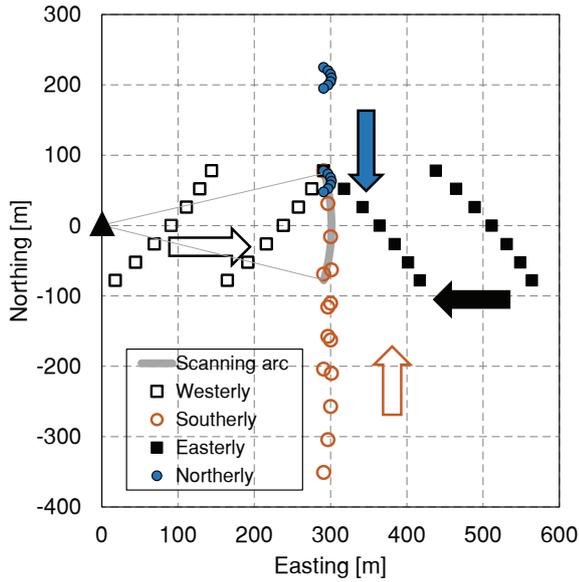
Figure 2. An example of the spatial distribution of air parcels sampled in two consecutive arc scans by a lidar at range distance $s = 315\,\text{m}$ for four different wind directions (westerly, easterly, northerly, and easterly) under the following assumptions: (1) frozen turbulence, (2) the lidar is located at the origin (the dark triangle) scanning from $\theta = 75$ to $105°$ with $5°$ increments with elevation angle $\phi = 17°$, (3) the mean wind speed is $7\,\text{m s}^{-1}$ and (4) the sampling interval is 3 s.

entry of $\mathbf{A}$ at ith row and jth column is defined by Eq. (4). For a given scanning geometry, Eqs. (4) and (5) show that, apart from the atmospheric turbulence structure, the statistics of the measured radial velocities are controlled by the mean wind field because the separation distance $\Delta \boldsymbol{p}_{ij}$ or $\Delta \boldsymbol{q}_{ij}$ varies with the mean wind speed and direction (as illustrated in Fig. 2). When the relative direction of the lidar beam $\beta = 0°/180°$ (westerly/easterly in Fig. 2), the samples are located in a rectangular area swept by the wind over the arc. When $\beta = \pm 90°$, the samples are from a line aligned with the arc. If the scan direction is the same as the wind (i.e., $\beta = +90°$), the samples from one arc scan are clustered and almost from the same location (northerly in Fig. 2). When $\beta = -90°$, the locations sampled by one arc are more spatially extended (southerly in Fig. 2).

The uncertainty in the wind velocity estimated from arc scans can be derived from the covariance matrix $\mathbf{A}$ of the measured radial velocities. Assuming a horizontally homogeneous wind field with zero mean vertical wind speed (i.e., $w_0 = 0$), the solution of the ordinary least squares (V_1) based on Eq. (1) is the estimate of horizontal wind velocity (Wang et al., 2015):

$$V_1 = \mathbf{G} \boldsymbol{v}_{\mathrm{R}}, \tag{6}$$

where $\mathbf{G} = (\mathbf{D}^{\mathrm{T}} \mathbf{D})^{-1} \mathbf{D}^{\mathrm{T}}$ and $\boldsymbol{v}_{\mathrm{R}}$ is a vector including N radial velocities measured in, for example, 10 min. The

matrix $\mathbf{D}$ is a $N \times 2$ matrix with its ith row given by $[\cos\phi \sin\theta_i, \cos\phi \cos\theta_i]$. The estimated wind velocity V_1 comprises horizontal components, $V_1 = (u_1, v_1)$. The uncertainty in V_1 is characterized by its covariance matrix ($\mathbf{C}_1$) given by

$$\mathbf{C}_1 = \mathbf{G} \mathbf{A} \mathbf{G}^{\mathrm{T}}, \tag{7}$$

assuming zero random error for radial velocity (Wang et al., 2015). The variance of the random error σ_e^2 is $\sim 0.01\,\text{m}^2\,\text{s}^{-2}$ (see Sect. 2) which is much smaller than the diagonal terms of $\mathbf{A}$ ($> 0.1\,\text{m}^2\,\text{s}^{-2}$ given wind speed $> 4\,\text{m s}^{-1}$ and turbulence intensity $\approx 10\,\%$); therefore, it can be neglected. For most applications, the desired output from arc scans is the horizontal wind speed (V_1) that is estimated as

$$V_1 = \sqrt{u_1^2 + v_1^2}. \tag{8}$$

The uncertainty in V_1 as quantified by the standard error (σ_1) can be approximated as (Lyons, 1991):

$$\sigma_1 = \left[(u_1 \sigma_{\mathrm{lu}})^2 + (v_1 \sigma_{\mathrm{lv}})^2 + 2(\rho_{uv} \sigma_{\mathrm{lu}} \sigma_{\mathrm{lv}})(u_1 v_1) \right]^{0.5} / V_1, \tag{9}$$

where σ_{lu}^2 and σ_{lv}^2 represent the variance of u_1 and v_1 and can be found from the diagonal of $\mathbf{C}_1$, respectively. The term ρ_{uv} in Eq. (9) is the correlation between u_1 and v_1, and $\rho_{uv} \sigma_{\mathrm{lu}} \sigma_{\mathrm{lv}}$ is the covariance that is given by the only non-diagonal term in $\mathbf{C}_1$. The value of σ_1 can be estimated from the observational data using Eq. (7) with the diagonal terms in $\mathbf{A}$ being approximated by v_{R} variance derived from measurements and the off-diagonal terms being zero (i.e., assuming no correlation between the measured radial velocities) (Wang et al., 2015).

4   Uncertainty computed from an isotropic turbulence model

Following the background presented in Sect. 3 above, the uncertainty in a 10 min mean wind speed estimated from lidar arc scans is analyzed as a function of (1) turbulence intensity, (2) mean wind speed and direction, and (3) scanning geometry using an isotropic turbulence model. For isotropic turbulence the covariance of the measured radial velocities in Eq. (4) can be calculated as follows: the entry at the lth row and kth column ($l, k = 1, 2, 3$) of the covariance matrix $\mathbf{C}(\boldsymbol{q})$ in Eq. (5) is given by the following equation (Monin and Yaglom, 1965)

$$c_{\mathrm{lk}}(\boldsymbol{q}) = c_u(q)\delta_{lk} + \frac{1}{2} q \frac{\mathrm{d}c_u}{\mathrm{d}q} \left(\delta_{\mathrm{lk}} - \frac{q_l q_k}{q^2} \right), \tag{10}$$

where $q = |\boldsymbol{q}|$, q_1, q_2 and q_3 are the separation distances in the streamwise, transverse and vertical directions, respectively, and δ_{lk} is the Kronecker delta. The streamwise wind component spatial covariance function $c_u(q)$ can be approximated by the exponential decay function

$$c_u(q) = \sigma_u^2 \exp\left(-\frac{q}{L_u} \right), \tag{11}$$

where σ_u^2 is the streamwise velocity variance, and L_u is the turbulence integral length scale which can be calculated from turbulence intensity (TI $= \sigma_u/V_0$) in a neutrally stratified atmospheric boundary layer (see Appendix A). Note that Eq. (11) misrepresents properties of turbulence of small scales and thus is not consistent with the von Kármán model used to calculate L_u in Appendix A, but it has similar accuracy to the von Kármán model in predicting the uncertainty of wind speed from conical scans (Banakh et al., 1995). Thus, Eq. (11) is used here for its simplicity and effectiveness. For a given wind speed and direction, the separation distance vector $\boldsymbol{q}$ can be calculated from ϕ, $\delta\theta$ and r, and the point radial velocity covariance defined in Eq. (5) can be derived from Eqs. (10) and (11). Then the covariance of the measured radial velocities can be calculated by defining a weighting function in Eq. (4). In this analysis the weighting function is approximated by a triangular weighting function defined as

$$W(r-s) = \max\left[0, \frac{2}{\Delta R}\left(1 - \frac{2}{\Delta R}|r-s|\right)\right], \quad (12)$$

where ΔR is the spatial extent of v_R along the LOS, which is a function of the lidar pulse length and hence the illuminated volume at the time of measurement. For the Galion $\Delta R = 60$ m according to Frehlich (1997) and the lidar parameters in Table 1. The radial velocity covariance matrix **A** in Eq. (7) is calculated for N measured radial velocities and used in Eq. (9) for calculation of the associated uncertainty in V_1 which is presented here as the relative standard error (abbreviated as lidar RSE and denoted by ε_1) defined as the ratio of the standard error of the estimated mean horizontal wind speed (σ_1) to the true mean horizontal wind speed (V_0):

$$\varepsilon_1 = \frac{\sigma_1}{V_0}. \quad (13)$$

The magnitude of ε_1 is a function of TI, mean wind speed and direction. Note that ε_1 is inversely proportional to $\Delta R/L_u$ which determines the amount of averaging taken for v_R (see Eq. 3). For a given L_u, a larger ΔR implies an average over a bigger area, and therefore less variation in the measured radial velocity and less uncertainty in the estimated wind velocity. Because L_u is defined as a function of TI and height (see Appendix A) and only one lidar with a constant ΔR is investigated here, the dependence of ε_1 on $\Delta R/L_u$ is not considered hereafter.

The relative importance of these functional dependencies and relevance to wind energy applications can be demonstrated using an example in which a lidar is used for a power performance test of a turbine. This type of test is undertaken to determine if the turbine is operating according to the specified power curve (i.e., production of electricity as a function of the inflow wind speed) and thus it involves measurements of the incident flow into the turbine rotor (Wagner et al., 2011). When lidars are used for this purpose they are typically deployed to measure with arc scans at the hub
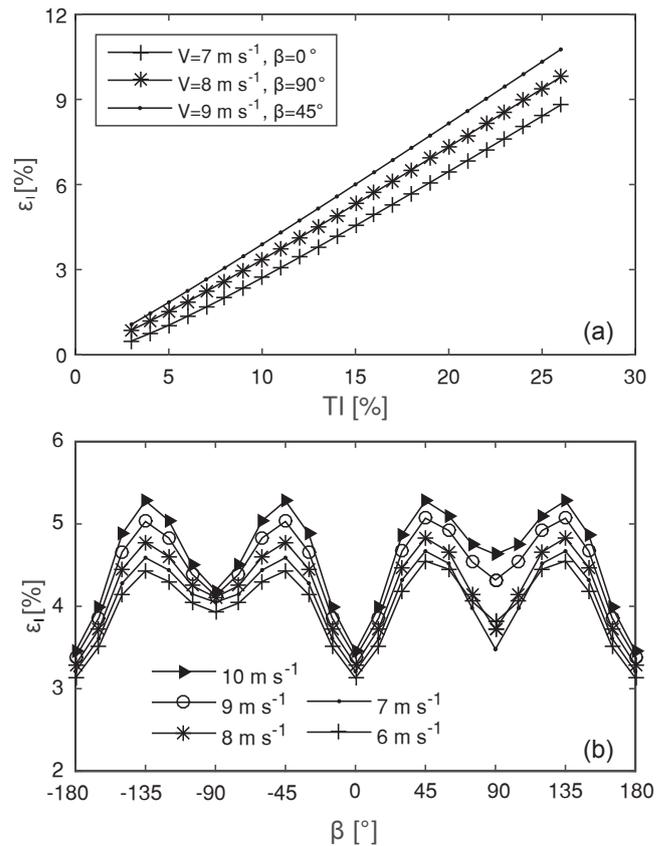
Figure 3. Dependence of the relative standard error (ε_1) of wind speed estimated from arc scans on **(a)** turbulence intensity (TI) and **(b)** wind speed (V_0) and direction (expressed as the relative direction (β)) based on the isotropic turbulence model given in Eq. (10) for the following scan geometry: $\phi = 16.7°$, $\Delta\theta = 30°$, $\delta\theta = 6°$ and $r = 313$ m. The Coriolis parameter $f_0 = 0.0001$ s^{-1}.

height 2–4 rotor diameters in front of the wind turbine (IEC, 2005). Assuming that the hub height is 90 m, the rotor diameter is 90 m, and the lidar placed at the base of the turbine is operated with a fixed elevation angle of 16.7° to measure wind velocities 3 rotor diameters in front of the turbine at hub height (i.e., $r = 313$ m). The arc scan is defined using a span of $\Delta\theta$ comprising M_θ azimuth angles. It takes δt s to finish one measurement at one azimuth angle and move $\delta\theta$ to the next azimuth angle, so the sampling intervals are δt in time and $\delta\theta$ in space. As a result, one arc scan takes $M_\theta \delta t$ s and the total number of arc scans conducted in 10 min is $M_{10} = 600/M_\theta \delta t$. For the power performance test scenario described above typical parameters would be: $\delta t = 3$ s, $\Delta\theta = 30°$ and $\delta\theta = 6°$. For reasonable values of TI and V_0, using the isotropic turbulence model and the definition of the dominant length scale L_u in Appendix A, RSE (ε_1) shows strongest dependence on TI (Fig. 3a), and increases from about 1.5 % for $V_0 = 7$–9 m s^{-1} at TI $= 5$ % (a low turbulence environment such as might be experienced offshore) to 6–9 % for TI > 20 % (i.e., a high turbulence en-

vironment). RSE also increases with increasing wind speed through its relationship with the variance. The RSE (ε_1) for TI = 12 %, for a range of wind speed (V_0) and relative direction (β) from −180 to 180°, indicates that under the assumption of isotropic turbulence ε_1 varies with β but the variation is no more than ±2 % for the range of conditions shown in Fig. 3b. The relationships shown in Fig. 3b are expected because the sample locations and resulting spatial correlations between the samples are determined by wind speed and direction (see Fig. 2). RSE reaches its minimum at $\beta = 0$ and 180° and exhibits the lowest dependence on wind speed. The maximum ε_1 occurs at $\beta = \pm45$ and ±135° and exhibits a much stronger dependence on wind speed. When $\beta = \pm90$°, ε_1 reaches local minima and has a relatively large difference between $\beta = -90$° and $\beta = +90$° because of the different spatial distribution and thus spatial correlation of samples between $\beta = -90$° and $\beta = +90$° (see Fig. 2). The effect of scanning geometry on ε_1 is such that ε_1 decreases with increasing arc span ($\Delta\theta$) and decreasing beam number (or azimuth angles) per arc scan (Fig. 4). Enlarging $\Delta\theta$ increases the spatial coverage, and lowering the number of beams per arc scan increases the separation distance between samples, both of which reduce the correlation between samples and consequently the uncertainty in the estimated horizontal mean wind speed. Additionally, when $\Delta\theta$ increases and beam number decreases, the condition number of the matrix **G** in Eq. (6) decreases and, as a result, the uncertainty introduced by the inverse method (least squares method) decreases (Wang et al., 2015). The effect of scanning geometry on ε_1 naturally exhibits a dependence on the relative direction (β). When the wind direction is parallel to the beams ($\beta = 0$°), ε_1 is weakly dependent on both arc span and beam number (Fig. 4a). For example, with a fixed beam number, ε_1 decreases by only 0.4 % when increasing $\Delta\theta$ from 30 to 120°. When $\beta = \pm45$°, ε_1 is less sensitive to beam number than arc span (Fig. 4b). When $\beta = \pm90$°, ε_1 is more sensitive to beam number than arc span (Fig. 4c and d). Sensitivity is highest when $\beta = +90$° and $\Delta\theta < 60$°. When $\beta = +90$°, there is a band of local minima with $\varepsilon_1 < 4$ % starting at $\Delta\theta = 30$° and beam number 8. The beam numbers and the arc spans associated with those minima are such that the distance between two adjacent azimuth angles is equal to the distance that wind travels when the lidar changes from one azimuth angle to the next one. In other words, under the frozen turbulence assumption the lidar samples the same location repetitively, causing the uncertainty to reduce. The uncertainty in wind speed derived from arc scans naturally causes uncertainty in determining the wind speed corresponding to a power output and consequently uncertainty in the measured power curve. If the power coefficient of the wind turbine is invariant with wind speed, the uncertainty in the measured power curve is $3\varepsilon_1$ (because wind power is proportional to the cube of wind speed). Hence, neglecting other sources of uncertainty and error in wind turbine power performance test, such as shear across the swept area (Wagner
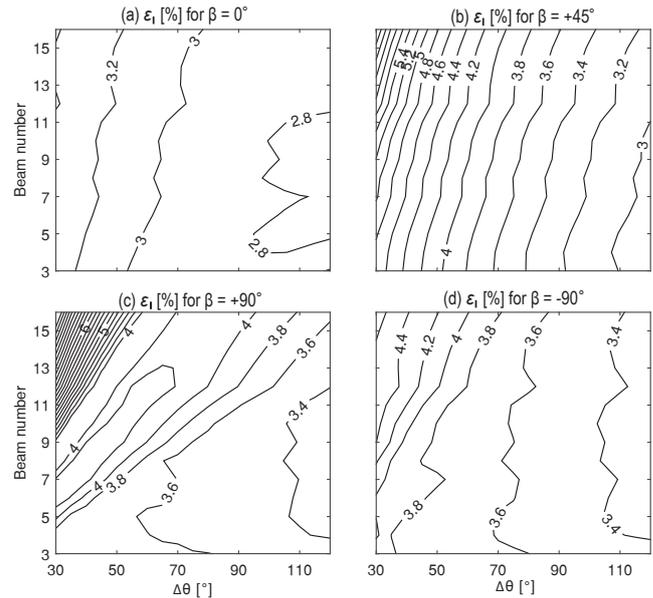

Figure 4. Dependence of relative standard error (ε_1) of wind speed (V_0) on arc span ($\Delta\theta$) and beam number per arc scan for relative directions **(a)** $\beta = 0$°, **(b)** $\beta = +45$°, **(c)** $\beta = +90$°, and **(d)** $\beta = -90$° with $\phi = 16.7$° and $r = 313$ m. The results are calculated for $V_0 = 7$ m s^{-1} and TI = 12 % over a 10 min period. The Coriolis parameter $f_0 = 0.0001$ s^{-1}. The contour interval is 0.2 %.

et al., 2011), the analyses presented above imply that if the lidar beam is well aligned with the incoming "free stream", the uncertainty in the measured power curve derived from the wind speed measurement by lidar for this example turbine and wind speeds of 7–9 m s^{-1} is about ±4 % for a site with low turbulence intensity (TI = 5 %) and ±20 % for a high turbulence intensity environment (TI = 20 %). Though these values of uncertainty resulting from lidar arc scans are similar to the uncertainties in the power curve measured with cup anemometers with the same turbulence characteristics (Wyngaard, 2010), using lidar arc scans can eliminate the uncertainty of cup anemometer measurements caused by meteorological mast flow distortion, which has a typical value of ±1 % in wind speed and therefore ±3 % in wind power (IEC, 2005).

5 Observed arc scan uncertainty

The theoretical uncertainty from the isotropic turbulence model presented in the previous section is a useful tool for decomposing the uncertainty by source, and potentially to aid in planning lidar scan geometries prior to on-site deployment. It is used here to contextualize empirical analyses of the uncertainty on the mean wind velocity, turbulence statistics and scanning geometry using observational data derived from arc scans at three sites. Site names are not revealed because of confidentiality, but the site characteristics
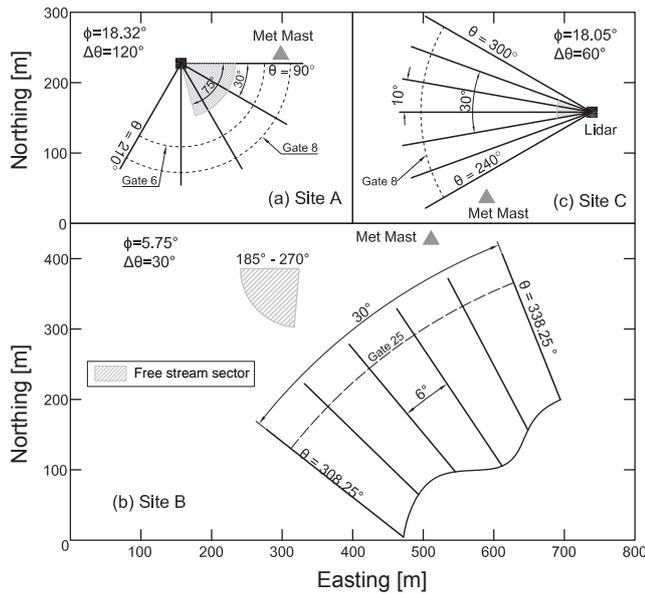
Figure 5. Plan views of the scanning geometries used at **(a)** Site A, **(b)** Site B and **(c)** Site C. The dark squares indicate the lidar locations, and the hatched areas indicate the wind direction sectors without flow distortions. Locations of meteorological masts are denoted by the solid gray circles. The elevation angle (ϕ) and the arc span ($\Delta\theta$) used at each of the sites are also given.

Table 2. Uncertainty classification of the cup anemometers used at the three sites.

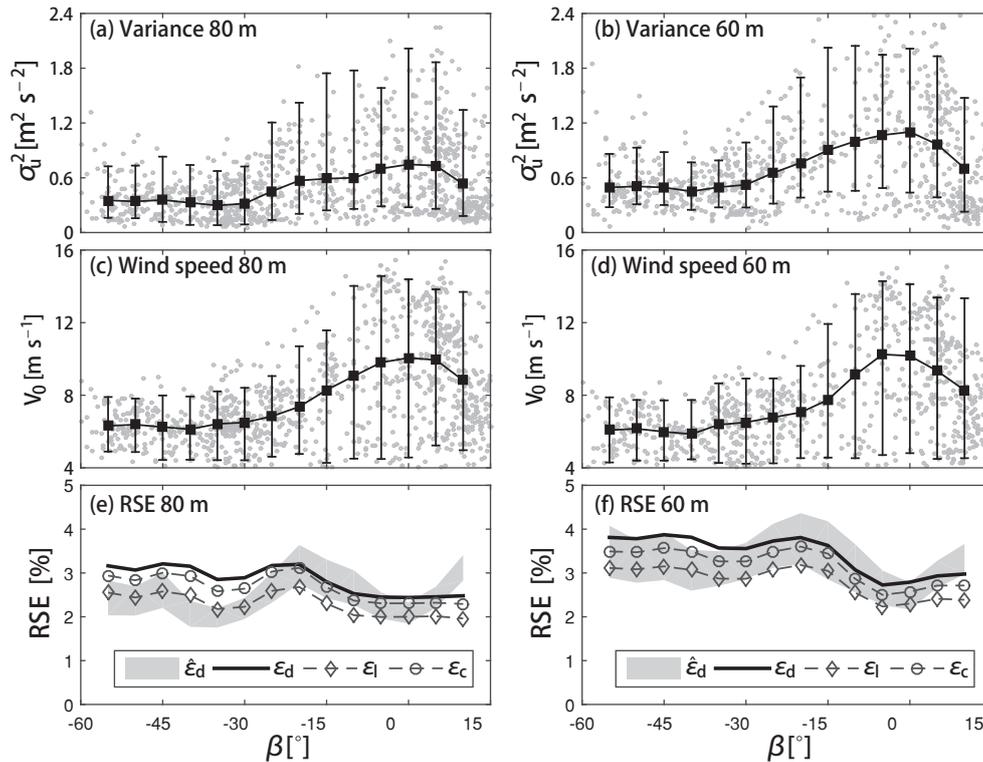| Site	Cup Anemometer	IEC Class[1]	Class Number
Site A	NRG 40C	A	2.40[2]
Site B	Vector L100	A	1.80[2]
Site C	WindSensor P2546A	B	3.71[3]

[1] Class A is for sites with flat terrain and Class B is for sites with complex terrain (IEC, 2005). [2] Pedersen et al. (2006). [3] Cup anemometer manufacturer.

Terms on the right hand side (RHS) of Eq. (16) represent sources of errors and will be estimated as follows in order to differentiate the lidar RSE from the difference between lidar and cup anemometer measurements:

– ε_l is the lidar RSE due to turbulence defined in Eq. (13) that can be estimated with the isotropic turbulence model.

– ε_c is the cup RSE due to turbulence, which is a function of the integral time scale and the sampling duration (Lenschow et al., 1994). Equation (13) in Lenschow et al. (1994) will be used to estimate ε_c by assuming that the streamwise velocity autocorrelation decays exponentially. The integral time scale is derived from the integral length scale (L_u) in Eq. (A12) and the observed mean wind speed. The sampling duration is 10 min.

– ρ_{lc} is the correlation between the turbulence-related errors of lidar and cup anemometers that depends on the spatial structure of turbulence and the distance between cup and lidar measurement locations. Estimating ρ_{lc} is difficult because lidar measures a volume and cup measures a point (or a line assuming frozen turbulence). A simple approximation is used here to estimate ρ_{lc}. The separation distance is the distance between the center of an arc and the cup location which are 150 m for both Site A and Site B and 120 m for Site C. The correlation decays exponentially with the same integral length scale that is used to estimate ε_l and ε_c at each site.

– ε_{cup} is the instrument error that can be found from the following equation:

$$\varepsilon_{cup} = \left(\frac{k}{\sqrt{3}}\right) \cdot \left(\frac{0.05\,\mathrm{m\,s^{-1}}}{V_0} + 0.005\right), \qquad (17)$$

where k is the cup anemometer class number that represents the maximum relative error of a cup anemometer in turbulent wind fields (IEC, 2005; Pedersen et al., 2006). The k values for cup anemometers used at the three sites are listed in Table 2.

are provided below and the scan geometries are summarized in Fig. 5. In all cases the analysis is based on the estimated 10 min horizontal mean wind speed (V_l) from the Galion measurements as derived using the ordinary least squares method. The RSE of V_l will be evaluated through the relative difference (e_d) between V_l and the measurement (V_c) from cup anemometers installed on nearby meteorological masts (in compliance with the standard, IEC, 2005):

$$e_d = \frac{V_l - V_c}{V_c}. \qquad (14)$$

Periods with $V_c < 4\,\mathrm{m\,s^{-1}}$ or lidar SNR $< -20\,\mathrm{dB}$ are excluded from the analysis. To quantify the measurement uncertainty, the observed RSE ($\hat{\varepsilon}_d$) is defined as the standard deviation of e_d binned by wind direction or turbulence intensity, and the 95 % confidence interval, CI$_{95}$, of $\hat{\varepsilon}_d$ is estimated by (Ahn and Fessler, 2003):

$$\mathrm{CI}_{95} = \hat{\varepsilon}_d \pm 1.96\hat{\varepsilon}_d/\sqrt{2(n-1)}, \qquad (15)$$

where n is the number of samples in a bin. Note that this definition means that only the spread of values is evaluated and bias is not considered.

The value of $\hat{\varepsilon}_d$ has contributions from random errors related to both instrument and turbulence. The lidar instrument errors are not considered; hence, the expected RSE (ε_d) based on the relative difference between lidar and cup anemometer measurements has the following definition:

$$\varepsilon_d^2 = \varepsilon_l^2 + \varepsilon_c^2 - 2\rho_{lc}\varepsilon_l\varepsilon_c + \varepsilon_{cup}^2. \qquad (16)$$

Figure 6. Variation of the standard error (RSE) with the relative direction (β) at Site A at 80 m height in **(a, c, e)** and 60 m height in **(b, d, f)**. The RSE is given in **(e, f)** for the 95 % confidence interval of the observed difference between the cup and lidar measurements ($\hat{\varepsilon}_\mathrm{d}$), the predicted difference between the cup and lidar measurements (ε_d), the predicted cup error (ε_c), and the predicted lidar error (ε_l). The input for the RSE predictions include the mean wind speeds (V_0) shown in **(c, d)** and the mean wind speed variance (σ_u^2) shown in **(a, b)** for 80 m height and 60 m height, respectively.

5.1 Site A

Site A is a wind farm on a flat barren land, approximately 20 km from a coastline and at latitude 27° N. The Galion lidar was operated for 20 days with arc scans centered at $\theta = 150°$ with $\Delta\theta = 120°$, $\delta\theta = 30°$ and $\phi = 18.32°$ (Fig. 5a). Wind speeds estimated from arc scan measurements at range gate 6 and 8 are evaluated against the concurrent data from cup anemometers installed on booms aligned southwest (227°) at 60 m height and 80 m height on a meteorological mast east of the lidar, respectively (Fig. 5a). Because of flow distortions from the wind turbines and the meteorological mast, the uncertainty evaluation is conducted only in the wind direction sector 90–165° (based on the wind vane measurement at 77 m on the meteorological mast), resulting in 952 and 775 measurements of 10 minute mean wind speeds at 80 and 60 m height, respectively, and 100 % recovery rate at both heights.

The observed RSE of relative difference ($\hat{\varepsilon}_\mathrm{d}$) is calculated for 10° bins of β with V_c between 4 and 16 m s^{-1}, and all terms on the RHS of Eq. (16) are estimated using the mean and variance of wind speed in each bin. The cup (ε_c) and lidar (ε_l) RSE show similar dependence on the relative direction (Fig. 6), which is solely the result of variation of the mean and variance of wind speed with the relative direction. The directional dependence of arc scan RSE mentioned in Sect. 4 should be negligible because of the large arc span applied here. The fact that $\varepsilon_\mathrm{l} < \varepsilon_\mathrm{c}$ in all direction bins (Fig. 6) supports the advantage of using large $\Delta\theta$ for arc scans. A large $\Delta\theta$ allows averaging over a large area, reducing the random error of mean wind speed. The expected RSE (ε_d), which combines both ε_l and ε_c based on Eq. (16), agrees well with the observed RSE ($\hat{\varepsilon}_\mathrm{d}$) except for some overestimation when $\beta < -20°$ at 80 m height (Fig. 6). The consistency between $\hat{\varepsilon}_\mathrm{d}$ and ε_d at Site A indicates that turbulent wind fluctuations are the main source of uncertainty and those assumptions made in applying the isotropic turbulence model are largely realized.

5.2 Site B

Site B is an offshore wind farm at latitude 54.0° N at which the Galion lidar made arc scans for three months centered at $\theta = 323.25°$ with $\Delta\theta = 30°$, $\delta\theta = 6°$ and $\phi = 5.75°$. Wind speeds retrieved from range gate 25 are evaluated against concurrent cup anemometer measurements collected on a boom oriented at 135° at 90 m on the meteorological mast north-northwest of the lidar (Fig. 5b). Observa-
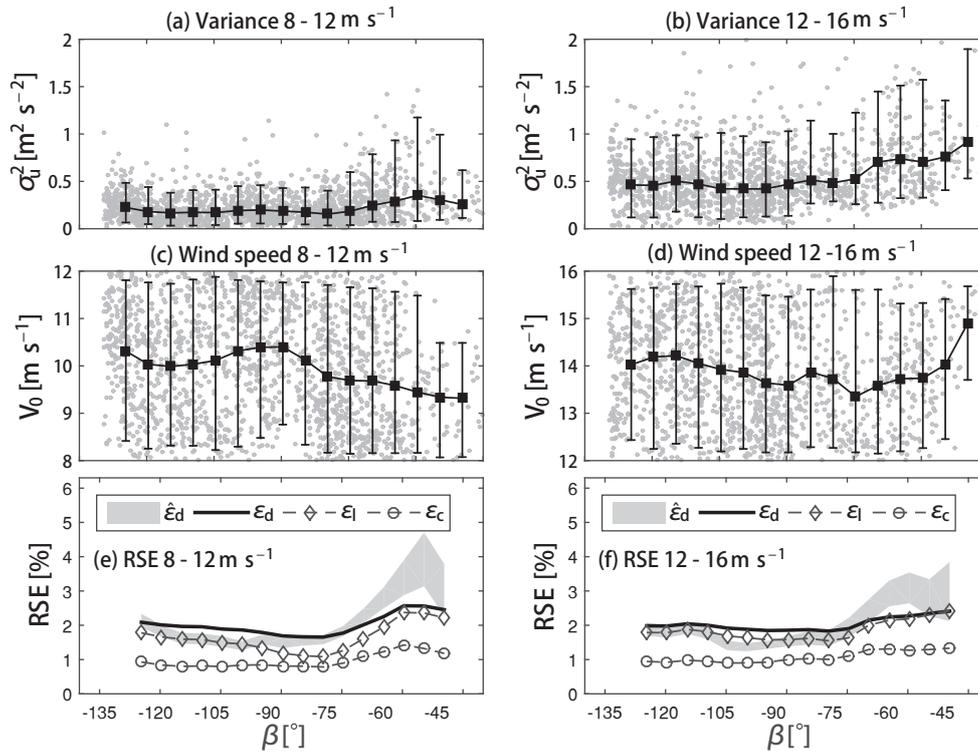
Figure 7. Variation of the standard error (RSE) with the relative direction (β) at Site B for the wind speed bin 8–12 m s^{-1} in **(a, c, e)** and the wind speed bin 12–16 m s^{-1} in **(b, d, f)**. The RSE is given in **(e, f)** for the 95 % confidence interval of the observed difference between the cup and lidar measurements ($\hat{\varepsilon}_d$), the predicted difference between the cup and lidar measurements (ε_d), the predicted cup error (ε_c), and the predicted lidar error (ε_l). The input for the RSE predictions include the mean wind speeds (V_0) shown in **(c, d)** and the mean wind speed variance (σ_u^2) shown in **(a, b)** for the wind speed bin 8–12 and 12–16 m s^{-1}, respectively.

tions within a wind direction sector 185–270° (2954 measurements of 10 min mean wind speeds with 97 % data recovery rate) are used for analysis because of flow distortion from the wind turbines and the meteorological mast in the other sectors.

Data are stratified into two wind speed bins 8–12 and 12–16 m s^{-1} (based on V_c), and are sampled in 10° bins of β. In general there is a good agreement between the observed ($\hat{\varepsilon}_d$) and expected (ε_d) RSE (Fig. 7). Due to the small arc span applied at Site B, ε_l has higher dependence than ε_c on the relative direction (β), and $\varepsilon_l > \varepsilon_d$ (Fig. 7). It seems that $\hat{\varepsilon}_d$ follows ε_l when β changes, while ε_c has little variation with β (Fig. 7). The high $\hat{\varepsilon}_d$ when $\beta > -70°$ is likely caused by the high values of ε_l, although there could be other contributors such as wind turbine wakes and low sample size.

5.3 Site C

Site C is a wind farm located at latitude 38.1° N in relatively complex terrain. Arc scans were performed over 25 days centered at $\theta = 270°$ with $\Delta\theta = 60°$, $\delta\theta = 10°$ and $\phi = 18.05°$ (Fig. 5c). Wind speeds retrieved from range gate 8 are evaluated against measurements from a cup anemometer deployed on a boom oriented to 247.5° at 80 m on the meteorological

mast southwest of the lidar (Fig. 5c). There is no flow distortion in the wind direction sector 205–290°. However, because of orographic channeling, 95 % of observations are associated with wind directions between 260 and 290°. Thus, this sector, which contains 2167 measurements of 10 min mean wind speed (93 % data recovery rate), is chosen for the uncertainty analysis.

Both observed ($\hat{\varepsilon}_d$) and expected (ε_d) RSE for 2° bins of β and wind speed between 6 and 14 m s^{-1} indicate a dependence on wind direction which derives largely from the directional variability of the mean and variance of wind speed (Fig. 8). $\hat{\varepsilon}_d$ increases from 2 % for $\beta \sim -10°$ to nearly 4 % at $\beta \sim +12°$ in large part due to the decrease in mean wind speed (from 11 to ~ 9 m s^{-1}) and increase in variance (from < 0.6 to nearly 1 m^2 s^{-2}). Though the agreement between $\hat{\varepsilon}_d$ and ε_d is good, both ε_l and ε_c are much lower than $\hat{\varepsilon}_d$. It is the instrument error of cup (ε_{cup}) that contributes the most to the difference between the lidar and cup measurements. The values of ε_l and ε_c are very close. Note that ε_l and ε_c should be lower than the actual values because non-homogeneous horizontal wind fields and non-zero vertical wind speeds over complex terrain violate assumptions in the theoretical models (Bingöl et al., 2009).
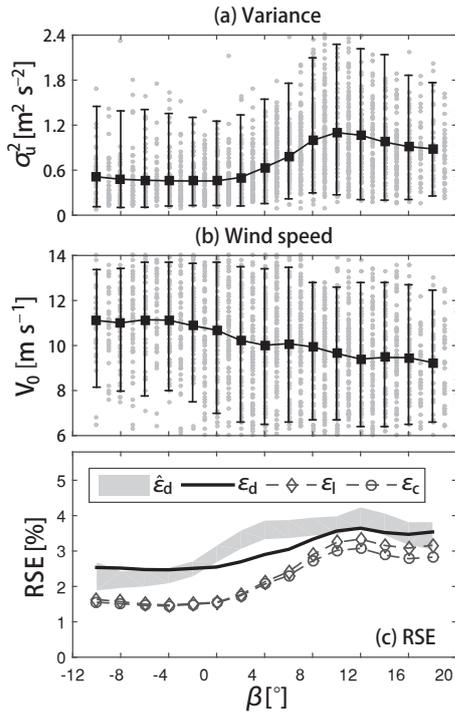
Figure 8. Variation of the standard error (RSE) with the relative direction (β) at Site C at 80 m height. The RSE is given in **(c)** for the 95 % confidence interval of the observed difference between the cup and lidar measurements ($\hat{\varepsilon}_d$), the predicted difference between the cup and lidar measurements (ε_d), the predicted cup error (ε_c), and the predicted lidar error (ε_l). The input for the RSE predictions include the mean wind speeds (V_0) shown in **(b)** and the mean wind speed variance (σ_u^2) shown in **(a)**.

6 Discussion

The isotropic turbulence model is not a true representation of the turbulent wind field in the atmosphere. The three wind components rarely have equal variance and the same turbulence integral length scale. Further, the exponential decay function is only an approximation of the turbulence autocorrelation function. Nevertheless, the analyses presented above indicate that when properly constrained, the isotropic turbulence model reproduces the uncertainty in wind speed estimated from arc scans with different scanning geometries at different sites, and the predicted relationship between RSE and turbulence intensity is also consistent with the observed relationship (Fig. 9). The effect of the arc span on the uncertainty of wind speed estimated from arc scans as presented based on the theoretical approach can also be verified by observations after they have been normalized to remove the effect of sample number, turbulence intensity and wind speed on the uncertainty to allow comparison across the sites. Thus the relative errors (e_d) are scaled using (Wyngaard, 2010):

$$e_{dN} = \frac{e_d}{S_1 \cdot S_2 \cdot S_3}, \tag{18}$$
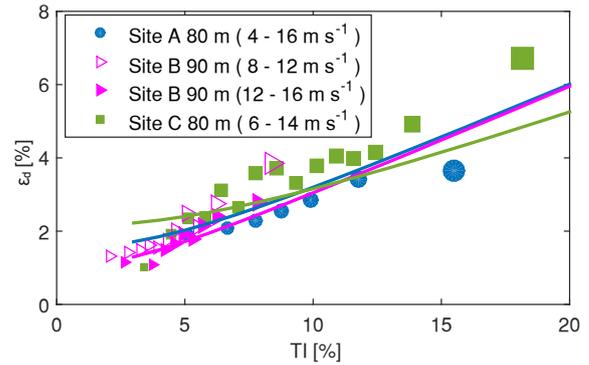
Figure 9. The relationship between the RSE of the relative difference between lidar and cup measurements (ε_d) and the turbulence intensity (TI) at the three sites. The 95 % confidence interval for each observed RSE ($\hat{\varepsilon}_d$) is denoted by the marker size. The solid lines with matching colors are the predicted relationships at the sites. Prediction at Site A uses wind speed $8\,\mathrm{m\,s^{-1}}$ and wind direction 150°, at Site B wind speed $10\,\mathrm{m\,s^{-1}}$ and wind direction 323°, and at Site C wind speed $10\,\mathrm{m\,s^{-1}}$ and wind direction 270°. Values of ε_d here are derived from the cup errors related to the turbulence (ε_c) and instrument (ε_{cup}), and the predicted lidar RSE (ε_l) according to Eq. (16) and Table 2.

where

- $S_1 = (M_{10})^{-1/2}$ represents the relationship between the uncertainty and the sample number M_{10} used to derive the mean horizontal wind speed.

- $S_2 = \mathrm{TI}$ accounts for the fact that the uncertainty scales with turbulence intensity.

- $S_3 = V_0 \cdot L_u / 600\,\mathrm{s}$ represents the spatial coverage of a measurement over 600 s (10 min) relative to the turbulence integral length scale.

The standard deviations of the errors, when e_{dN} is rescaled back to e_d with $V_0 = 9\,\mathrm{m\,s^{-1}}$, $\mathrm{TI} = 12\,\%$ ($L_u = 209\,\mathrm{m}$ according to Appendix A) and $M_{10} = 40$ using Eq. (18), are 2.0, 2.0 and 6.8 % after being corrected for ε_c and ε_{cup} according to Eq. (16) for Site A, Site C and Site B, respectively. In other words, the uncertainty increases when $\Delta\theta$ decreases from 120° at Site A to 30° at Site B, which is consistent with the predicted relationship between $\Delta\theta$ and RSE given in Fig. 4. This implies that the approach presented in Sects. 3 and 4 may be of great use for lidar scan geometry optimization for a given site. Note that the effect of β has not been removed in the rescaling because an overlapping bin of β with a sufficient sample number cannot be found at the three sites; therefore, the rescaling may change if β is considered.
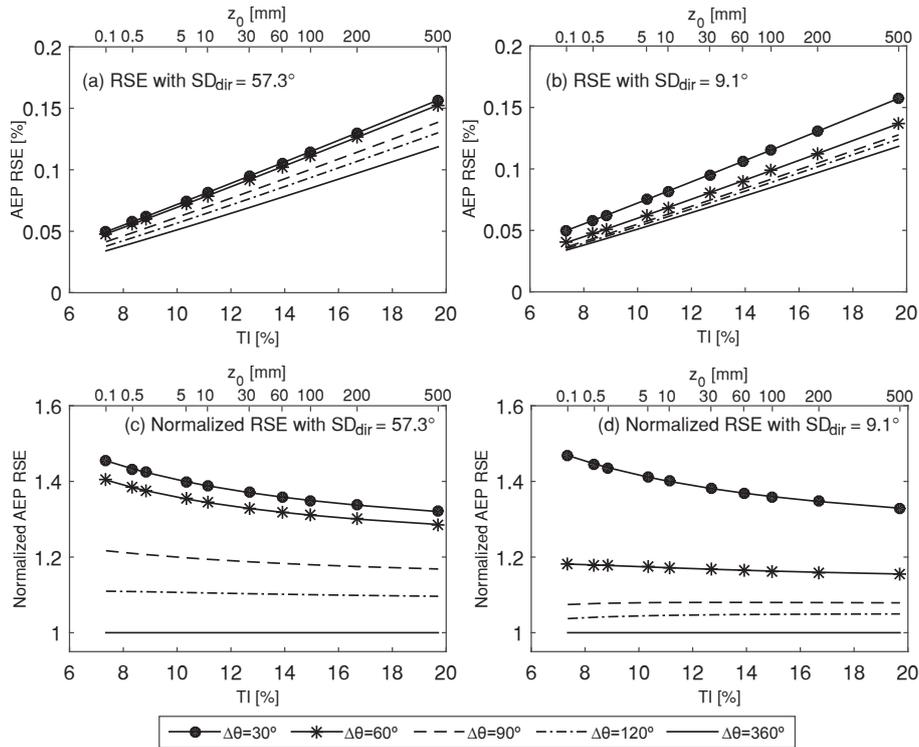
Figure 10. The relative standard error (RSE) in annual energy production (AEP) arising from arc scan velocity retrieval uncertainty as a function of turbulence intensity (TI) and surface roughness length (z_0), assuming that wind speed follows a Rayleigh distribution with a mean of $7\,\mathrm{m\,s^{-1}}$, and wind direction follows the von Mises distributions with a mean of 90° and standard deviations (SD$_{\mathrm{dir}}$) of 57.3° in (**a**) and 9.1° in (**b**). Four arc spans and a full azimuth conical scan (see the legend) are used for AEP prediction with six beams, $\phi = 15°$ and $r = 315\,\mathrm{m}$. The normalized AEP RSE, which is the ratio of predicted AEP RSE from arc scans to that from the conical scan, is shown in(**c**) for SD$_{\mathrm{dir}} = 57.3°$ and in (**d**) for SD$_{\mathrm{dir}} = 9.1°$.

7 Implications for applications in wind energy

If wind speed measurements deriving from arc scans of a lidar are used to predict annual energy production (AEP) at a given site, naturally, the uncertainty in wind speeds will propagate into AEP prediction and contribute to the uncertainty in wind resource assessment. The annual AEP is predicted as follows:

$$E_{\mathrm{y}} = \sum_{j=1}^{J}\sum_{i=1}^{I}(T_{\mathrm{y}}F_{\mathrm{V},i}F_{\mathrm{D},j})P_i, \tag{19}$$

where $F_{\mathrm{V},i}$ and $F_{\mathrm{D},j}$ are the probabilities of the ith wind speed bin and jth wind direction bin, respectively, P_i is the power production of a wind turbine at wind speed V_i, and T_{y} is the total hours in a year. Assuming statistical independence between lidar measurements, the contribution of the arc scan measurement uncertainty to the uncertainty of E_{y} is quantified by the standard error (σ_{y}) defined as follows (IEC 2005):

$$\sigma_{\mathrm{y}}^2 = \sum_{j=1}^{J}\sum_{i=1}^{I}(T_{\mathrm{y}}F_{\mathrm{V},i}F_{\mathrm{D},j})c_i^2\sigma_{1,ij}^2, \tag{20}$$

where $\sigma_{1,ij}$ is the lidar measurement standard error (see Eq. 9) for the ith wind speed bin and jth direction bin, and c_i is the sensitivity factor determined by

$$c_i = \left|\frac{P_i - P_{i-1}}{V_i - V_{i-1}}\right|. \tag{21}$$

A scenario analysis of the resulting uncertainty in AEP prediction is commenced under the following assumptions: (1) the wind speed follows a Rayleigh distribution with a mean of $7\,\mathrm{m\,s^{-1}}$, (2) the wind direction follows a von Mises distribution with a mean of 90° (see Appendix B for the probability density functions), (3) arc scans centered at $\theta = 90°$ with 6 beams, and $\phi = 15°$, and (4) the hub-height is 80 m. Turbulence intensity and turbulence integral length scale are estimated from surface roughness length using Eqs. (A3) and (A12) in Appendix A, respectively.

The uncertainty in AEP prediction calculated using Eq. (20) and a power curve from a commercial wind turbine is shown in Fig. 10 for different arc spans, wind direction distributions, and surface roughness length values. Because of the large number of samples used for AEP prediction ($T_{\mathrm{y}} = 8760$), the AEP RSE defined as $\sigma_{\mathrm{y}}/E_{\mathrm{y}}$ is very low (0.05–0.2 %). The uncertainty in AEP increases linearly with

TI (and hence z_0) and decreases with increasing arc span, but is not sensitive to the wind direction variation. The normalized AEP RSE, which is the ratio of the AEP RSE of arc scans to that of 6-beam conical scans (or $\Delta\theta = 360°$), has the highest value of about 1.4 for $\Delta\theta = 30°$ (Fig. 10c and d). Note the uncertainty of conical scans is the minimum value of uncertainty that arc scans can achieve (as a result of $\Delta\theta \rightarrow 360°$).

8   Conclusions

Wind speeds measured by lidars are subject to uncertainties that originate from prevailing atmospheric conditions, lidar scanning geometry and wind velocity retrieval method. The analyses presented herein assume horizontal homogeneity and zero mean vertical speed, and thus neglect their roles in dictating optimal lidar operation. The effects of atmospheric turbulence properties and scanning geometry on the uncertainty in the wind speed estimated from lidar arc scans are investigated with both theoretical predictions and actual observations. The theoretical predictions are based on the frozen turbulence hypothesis and an isotropic turbulence model, and the actual observations include arc scan measurements from different scanning geometries both onshore and offshore. The predictions and the observations are consistent, and may be summarized as follows.

- The uncertainty can be scaled with the turbulence intensity.

- The lowest uncertainty can be achieved by aligning the line of sight with the wind direction. The highest uncertainty occurs when the wind direction is 45° relative to the line of sight. There is a local minimum of uncertainty when the line of sight at the center of arc is orthogonal to the wind direction. However, it should be noted that radial velocities measured from orthogonal scans are zero.

- The uncertainty can generally be reduced by increasing arc span and decreasing beam number, although a minimum number of beams is required to characterize the wind velocity. The reduction is most significant when the relative angle between wind direction and line of sight is 45°. If the relative angle is close to zero, adjusting scan geometry will not change the uncertainty significantly. With orthogonal scans, the uncertainty is more sensitive to beam number than arc span.

- When arc scans are used for wind resource assessment, the uncertainty in annual energy production prediction arising from uncertainty in arc scan velocity retrieval is negligible. The uncertainty decreases with decreasing surface roughness and turbulence intensity, and increasing arc span.

The uncertainty estimation approach developed in this paper on the basis of the isotropic turbulence model, though is subject to limits and caveats, is able to predict the effect of wind velocity, turbulence intensity and scan geometry on the arc scan uncertainty at the three sites presented herein. Thus, this approach, although it needs to be further validated by more measurements, may have great utility for a priori optimization of lidar scan geometries for a given site.

Appendix A: Atmospheric boundary layer turbulence characteristics

In the neutrally stratified surface layer of the atmospheric boundary layer (ABL), the vertical profile of horizontal wind speed is given by the logarithmic wind profile (Stull, 1988):

$$V_0(z) = \frac{u_*}{\kappa} \ln\left(\frac{z}{z_0}\right), \tag{A1}$$

where u_* is surface friction velocity, z_0 is surface roughness length, $\kappa = 0.4$ is the von Kármán constant and z is height above the ground. The standard deviation of the horizontal wind speed (σ_u) normalized by the friction velocity is a constant; that is,

$$\frac{\sigma_u}{u_*} = c_n, \tag{A2}$$

where constant $c_n = 2.5$ (Stull, 1988). Hence, according to Eqs. (A1) and (A2), turbulence intensity, defined as $\mathrm{TI} = \sigma_u / V_0$ can be estimated using the following equation:

$$\mathrm{TI} = \frac{c_n \kappa}{\ln(z/z_0)}. \tag{A3}$$

The turbulence integral length scale is defined as

$$L_u = \frac{1}{\sigma_u^2} \int\limits_0^{+\infty} c_u(p)\,\mathrm{d}p, \tag{A4}$$

where c_u is the spatial covariance function of streamwise velocity. Based on the von Kármán model and the Kolmogorov's 5/3 law, for turbulence with high wave numbers (e.g., turbulence in the inertial subrange), L_u in the atmospheric surface layer (L_{us}) is defined as

$$L_{us} = c_1 \frac{\sigma_u^3}{\varepsilon_T}, \tag{A5}$$

where $c_1 = 0.7$ (Banakh et al., 1995; Frehlich and Cornman, 2002). The turbulence kinetic energy dissipation rate (ε_T) is related to the dimensionless dissipation rate (ϕ_ε) via the following equation:

$$\varepsilon_T = \frac{\phi_\varepsilon u_*^3}{\kappa z}. \tag{A6}$$

For a neutrally stratified atmosphere $\phi_\varepsilon = 1$ (Panofsky and Dutton, 1984). Thus, combining Eqs. (A2), (A5) and (A6) yields a linear relationship between the turbulence integral length scale and height in the neutrally stratified surface layer:

$$L_{us} = c_1 c_n^3 \kappa z. \tag{A7}$$

The actual turbulence integral length scale in the ABL is constrained by the ABL height (z_i) and the following equation can be used to account for the effect of z_i on L_u:

$$L_u(z) = \frac{L_{us}(z)}{1 + c_2 \frac{L_{us}(z)}{z_i}}, \tag{A8}$$

where $c_2 = 2.5$ (Blackadar, 1962; Banakh et al., 1995). The height of the neutrally stratified ABL can be determined using the following equation:

$$z_i = c_z \frac{u_*}{f_0}, \tag{A9}$$

where the coefficient $c_z = 0.07$–0.3 in the literature (Seibert et al., 2000) and we use $c_z = 0.3$ in this paper. The term f_0 is the Coriolis parameter and defined as

$$f_0 = 2\Omega \sin\phi_L, \tag{A10}$$

where ϕ_L is the latitude and $\Omega = 7.292 \times 10^{-5}\,\mathrm{rad\,s^{-1}}$ is the angular speed of the Earth. Combing Eqs. (A2), (A7) and (A8) yields the following formula:

$$L_u = \frac{c_1 c_n^3 \kappa z}{1 + \frac{\kappa c_1 c_2 c_n^4}{c_z} \frac{f_0 z}{\sigma_u}}. \tag{A11}$$

Using the values assigned to these empirical coefficients, L_u can be calculated using the following equation:

$$L_u = \frac{4.375 z \sigma_u}{\sigma_u + 91.146 f_0 z}. \tag{A12}$$

Appendix B: Wind speed and direction probability distributions

The wind speed distribution can be modeled using the Rayleigh distribution with the following probability density function (Forbes et al., 2011):

$$f_V(V) = \frac{2V}{A^2} \exp\left[-\left(\frac{V}{A}\right)^2\right], \tag{B1}$$

where A is the scale factor.

The wind direction distribution can be modeled by the von Mises distribution with the following probability density function (Forbes et al., 2011):

$$f_D(D) = \frac{\exp[b\cos(D - \overline{D})]}{2\pi I_0(b)}, \tag{B2}$$

where $D \in [0, 2\pi]$ is wind direction, $\overline{D}$ is the mean wind direction, b is the concentration parameter, and $I_0(\cdot)$ is the modified Bessel function of the first kind of order zero. The circular standard deviation (σ_D^2) of the wind direction is then defined as

$$\sigma_D^2 = 1 - I_1(b)/I_0(b), \tag{B3}$$

where $I_1(\cdot)$ is the modified Bessel function of the first kind of order one.

Appendix C

Table C1. Nomenclature.

$\mathbf{A}$	Covariance matrix of the measured radial velocities [m^2 s^{-2}]
A	Rayleigh distribution scale factor [m s^{-1}]
$\mathbf{C}$	Wind velocity covariance matrix [m^2 s^{-2}]
$\mathbf{C}_l$	Covariance matrix of the estimated horizontal wind vector [m^2 s^{-2}]
CI_{95}	95 % confidence interval
D	Wind direction [°]
$\mathbf{D}$	A $N \times 2$ matrix with its ith row given by [$\cos\phi\sin\theta_i \cos\phi\cos\theta_i$]
$\overline{D}$	Annual mean wind direction [°]
E_y	Annual energy production [J]
F_D	Wind direction probability
F_V	Wind speed probability
$\mathbf{G}$	A $2 \times N$ matrix defined as $(\mathbf{D}^T\mathbf{D})^{-1}\mathbf{D}^T$
$\mathbf{I}$	Identity matrix
I_k	Bessel function of the first kind of order k
K_r	Covariance between two point radial velocities [m^2 s^{-2}]
L_u	Turbulence integral length scale in the atmospheric boundary layer [m]
L_{us}	Turbulence integral length scale in the surface layer [m]
M_{10}	Number of arc scans over a 10 min period
M_θ	Number of azimuth angles per arc scan
N	Number of radial velocities measured over a 10 min period
P	Wind turbine power production [W]
T_y	Total hours in a year
$\mathbf{V}_l$	Estimated mean horizontal wind velocity vector from arc scans [m s^{-1}]
V_0	Horizontal mean wind speed [m s^{-1}]
V_l	Estimated horizontal mean wind speed from arc scans [m s^{-1}]
V_c	Horizontal mean wind speed from cup anemometers [m s^{-1}]
W	Lidar weighting function
a	Covariance between two measured radial velocities [m^2 s^{-2}]
b	von Mises distribution concentration parameter
c	Wind power sensitivity factor due to wind speed uncertainty [kg m s^{-2}]
c_{lk}	An entry of $\mathbf{C}$ [m^2 s^{-2}]
c_u	Spatial covariance of the streamwise wind component [m^2 s^{-2}]
$\boldsymbol{d}$	Unit directional vector of the line-of-sight of lidar
e	Radial velocity measurement random error [m s^{-1}]
e_d	Relative difference between lidar and cup anemometer measurements
e_{rd}	Normalized e_d
f_0	Coriolis parameter [s^{-1}]
f_D	Wind direction probability density function
f_V	Wind speed probability density function
k	Cup anemometer classification number
n	Number of samples
$\boldsymbol{p}$	Separation distance vector between two measured radial velocities [m]
$\boldsymbol{q}$	Separation distance vector between two point radial velocities [m]
q	Separation distance between two point radial velocities [m]
q_1	Separation distance in the streamwise direction [m]
q_2	Separation distance in the transverse direction [m]
q_3	Separation distance in the vertical direction [m]
$\boldsymbol{r}$	Lidar range gate position vector [m]
r	Lidar range gate location on the LOS [m]
$\boldsymbol{s}$	Point radial velocity position vector [m]
s	Point radial velocity location on the LOS [m]

Table C1. Continued.

$\boldsymbol{u}$	Instantaneous wind velocity vector [$\mathrm{m\,s^{-1}}$]
u	Instantaneous west–east wind component [$\mathrm{m\,s^{-1}}$]
$\boldsymbol{u}_0$	Mean wind velocity vector [$\mathrm{m\,s^{-1}}$]
u_0	Mean west–east wind component [$\mathrm{m\,s^{-1}}$]
u_l	Estimated mean west–east wind component [$\mathrm{m\,s^{-1}}$]
u_*	Surface friction velocity [$\mathrm{m\,s^{-1}}$]
v	Instantaneous south–north wind component [$\mathrm{m\,s^{-1}}$]
v_0	The mean south–north wind component [$\mathrm{m\,s^{-1}}$]
v_l	Estimated mean south–north wind component [$\mathrm{m\,s^{-1}}$]
$\boldsymbol{v}_\mathrm{R}$	Vector of the measured radial velocities over a 10 min period [$\mathrm{m\,s^{-1}}$]
v_R	Volumetrically averaged lidar radial velocity (measured) [$\mathrm{m\,s^{-1}}$]
v_R0	Volumetrically averaged lidar radial velocity (expected) [$\mathrm{m\,s^{-1}}$]
v_r	Point lidar radial velocity [$\mathrm{m\,s^{-1}}$]
w	Instantaneous vertical wind component [$\mathrm{m\,s^{-1}}$]
w_0	Mean vertical wind component [$\mathrm{m\,s^{-1}}$]
w_R	Lidar signal spectrum width in velocity space [$\mathrm{m\,s^{-1}}$]
z	Height [m]
z_i	Atmospheric boundary layer height [m]
ΔR	Spatial extent of a radial velocity measurement [m]
$\Delta \boldsymbol{p}$	Separation distance vector induced by the mean wind velocity [m]
$\Delta\theta$	Arc scan azimuth span [°]
Ω	Earth rotational speed [$\mathrm{s^{-1}}$]
β	Arc scan relative direction [°]
δ	Radial velocity measurement bias [$\mathrm{m\,s^{-1}}$]
δ_lk	the Kronecker delta
δt	Time interval between two radial velocity measurements [s]
$\delta\theta$	Arc scan azimuth angle interval [°]
ε_c	Relative standard error of cup anemometer due to turbulence
ε_cup	Relative standard error of cup anemometer due to instrument
ε_d	Relative standard error of the lidar and cup measurement difference
$\hat{\varepsilon}_\mathrm{d}$	Observed ε_d
ε_l	Relative standard error of lidar arc scan due to turbulence
ε_T	Turbulence kinetic energy dissipation rate [$\mathrm{m^2\,s^{-3}}$]
θ	Lidar azimuth angle [°]
ρ_{uv}	Correlation between u_l and v_l
ρ_lc	Correlation between lidar and cup measurements
σ_D	Wind direction standard deviation [°]
σ_e	Standard deviation of radial velocity measurement random errors [$\mathrm{m\,s^{-1}}$]
σ_l	Standard deviation of the estimated horizontal wind speed [$\mathrm{m\,s^{-1}}$]
σ_lu	Standard deviation of the estimated west–east wind component [$\mathrm{m\,s^{-1}}$]
σ_lv	Standard deviation of the estimated south–north wind component [$\mathrm{m\,s^{-1}}$]
σ_u^2	Variance of the streamwise wind component [$\mathrm{m^2\,s^{-2}}$]
σ_{v_r}	Standard deviation of radial velocities in the lidar probe volume [$\mathrm{m\,s^{-1}}$]
σ_y	Standard deviation of annual energy yield prediction [J]
ϕ	Lidar elevation angle [°]
ϕ_L	Latitude [°]
ϕ_ε	Dimensionless dissipation rate

Edited by: U. Wandinger

References

Ahn, S. and Fessler, J. A.: Standard Errors of Mean, Variance, and Standard Deviation Estimators, available at: http://ai.eecs.umich.edu/~fessler/papers/files/tr/stderr.pdf (last access: 1 October 2015), University of Michigan, Communication and Signal Processing Lab, Department of EECS, Ann Arbor, Michigan, 2003.

Aitken, M. L., Banta, R. M., Pichugina, Y. L., and Lundquist, J. K.: Quantifying wind turbine wake characteristics from scanning remote sensor data, J. Atmos. Ocean. Tech., 31, 765–787, doi:10.1175/JTECH-D-13-00104.1, 2014.

Banakh, V. A., Smalikho, I. N., Köpp, F., and Werner, C.: Representativeness of wind measurements with a cw Doppler lidar inthe atmospheric boundary layer, Appl. Optics, 34, 2055–2067, doi:10.1364/AO.34.002055, 1995.

Banta, R. M., Pichugina, Y. L., Kelley, N. D., Jonkman, B., and Brewer, W. A.: Doppler lidar measurements of the great plains low-level jet: applications to wind energy, IOP C. Ser. Earth Env., 1, 12–20, 2008.

Banta, R. M., Pichugina, Y. L., Kelley, N. D., Hardesty, R. M., and Brewer, W. A.: Wind energy meteorology: insight into wind properties in the turbine–rotor layer of the atmosphere from high-resolution Doppler lidar, B. Am. Meteorol. Soc., 94, 883–902, doi:10.1175/BAMS-D-11-00057.1, 2013.

Barthelmie, R. J., Crippa, P., Wang, H., Smith, C. M., Krishnamurthy, R., Choukulkar, A., Calhoun, R., Valyou, D., Marzocca, P., Matthiesen, D., Brown, G., and Pryor, S. C.: 3-D wind and turbulence characteristics of the atmospheric boundary layer, B. Am. Meteorol. Soc., 95, 743–756, doi:10.1175/BAMS-D-12-00111.1, 2013.

Bingöl, F., Mann, J., and Foussekis, D.: Conically scanning lidar error in complex terrain, Meteorol. Z., 18, 189–195, 2009.

Blackadar, A. K.: The vertical distribution of wind and turbulent exchange in a neutral atmosphere, J. Geophys. Res., 67, 3095–3102, doi:10.1029/JZ067i008p03095, 1962.

Calhoun, R., Heap, R., Princevac, M., Newsom, R., Fernando, H., and Ligon, D.: Virtual towers using coherent Doppler lidar during the Joint Urban 2003 Dispersion Experiment, J. Appl. Meteorol. Clim., 45, 1116–1126, doi:10.1175/JAM2391.1, 2006.

Choukulkar, A., Calhoun, R., Billings, B., and Doyle, J.: Investigation of a complex nocturnal flow in Owens Valley, California using coherent Doppler lidar, Bound.-Lay. Meteorol., 144, 359–378, 2012.

Courtney, M., Peña, A., Wagner, R., Peeringa, J., Brand, A., Gottschall, J., Rettenmeir, A., and Pierella, F.: D4.06 Data Reports and Databases: Data on Coastal and Offshore Wind Measurements, 42, available at: http://www.fp7-marinet.eu/public/docs/D4.06%20Data%20reports%20and%20databases.pdf (last access: 1 October 2015), MARINET, Cork, Ireland, 2014.

Forbes, C., Evans, M., Hastings, N., and Peacock, B.: Statistical Distributions, John Wiley & Sons, Hoboken, New Jersey, 230 pp., 2011.

Frehlich, R.: Effects of wind turbulence on coherent Doppler lidar performance, J. Atmos. Ocean. Tech., 14, 54–75, 1997.

Frehlich, R.: Estimation of velocity error for Doppler lidar measurements, J. Atmos. Ocean. Tech., 18, 1628–1639, 2001.

Frehlich, R. and Cornman, L.: Estimating spatial velocity statistics with coherent Doppler lidar, J. Atmos. Ocean. Tech., 19, 355–366, doi:10.1175/1520-0426-19.3.355, 2002.

Frehlich, R. and Yadlowsky, M.: Performance of mean-frequency estimators for Doppler radar and lidar, J. Atmos. Ocean. Tech., 11, 1217–1230, 1994.

Frehlich, R., Meillier, Y., Jensen, M. L., Balsley, B., and Sharman, R.: Measurements of boundary layer profiles in an urban environment, J. Appl. Meteorol. Clim., 45, 821–837, doi:10.1175/JAM2368.1, 2006.

Gottschall, J., Courtney, M. S., Wagner, R., Jørgensen, H. E., and Antoniou, I.: Lidar profilers in the context of wind energy – a verification procedure for traceable measurements, Wind Energy, 15, 147–159, doi:10.1002/we.518, 2012.

Henke, M. and Clive, P.: Robust low cost offshore power curve tests with LiDAR, in: EWEA Offshore 2015, 172, Copenhagen, Denmark, 10–12 March 2015.

IEC: IEC 61400-12-1: 2005 Wind turbines – Part 12-1: Power Performance Measurements of Electricity Producing Wind Turbines, Geneva, Switzerland, 90 pp., 2005.

Krishnamurthy, R., Calhoun, R., Billings, B., and Doyle, J.: Wind turbulence estimates in a valley by coherent Doppler lidar, Meteorol. Appl., 18, 361–371, doi:10.1002/met.263, 2011.

Krishnamurthy, R., Choukulkar, A., Calhoun, R., Fine, J., Oliver, A., and Barr, K. S.: Coherent Doppler lidar for wind farm characterization, Wind Energy, 16, 189–206, doi:10.1002/we.539, 2013.

Lenschow, D. H., Mann, J., and Kristensen, L.: How long is long enough when measuring fluxes and other turbulence statistics?, J. Atmos. Ocean. Tech., 11, 661–673, doi:10.1175/1520-0426(1994)011<0661:HLILEW>2.0.CO;2, 1994.

Lindelöw, P., Courtney, M., Parmentier, R., and Cariou, J.: Wind shear proportional errors in the horizontal wind speed sensed by focused, range gated lidars, IOP C. Ser. Earth Env., 1, 012023, doi:10.1088/1755-1315/1/1/012023, 2008.

Lyons, L.: A Practical Guide to Data Analysis for Physical Science Students, Cambridge University Press, Cambridge, UK, 95 pp., 1991.

Monin, A. S. and Yaglom, A. M.: Statistical Hydromechanics, Nauka, Moscow, 1965.

Panofsky, H. A. and Dutton, J. A.: Atmospheric turbulence: models and methods for engineering applications, John Wiley & Sons, New York, USA, 1984.

Pedersen, F. T., Dahlberg, J.-Å., and Busche, P.: ACCUWIND-Classification of Five Cup Anemometers According to IEC 61400-12-1, Forskningscenter Risøe, Denmark, Risøe-R, No. 1556(EN), 2006.

Pearson, G. N. and Collier, C. G.: A pulsed coherent CO_2 lidar for boundary-layer meteorology, Q. J. Roy. Meteor. Soc., 125, 2703–2721, doi:10.1002/qj.49712555918, 1999.

Pichugina, Y. L., Banta, R. M., Brewer, W. A., Sandberg, S. P., and Hardesty, R. M.: Doppler lidar-based wind-profile measure-

ment system for offshore wind-energy and other marine boundary layer applications, J. Appl. Meteorol. Clim., 51, 327–349, 2012.

Schwiesow, R., Köpp, P., and Werner, C.: Comparison of CW-lidar-measured wind values obtained by full conical scan, conical sector scan and two-point techniques, J. Atmos. Ocean. Tech., 2, 3–14, 1985.

Seibert, P., Beyrich, F., Gryning, S.-E., Joffre, S., Rasmussen, A., and Tercier, P.: Review and intercomparison of operational methods for the determination of the mixing height, Atmos. Environ., 34, 1001–1027, 2000.

Simley, E., Pao, L. Y., Frehlich, R., Jonkman, B., and Kelley, N.: Analysis of light detection and ranging wind speed measurements for wind turbine control, Wind Energy, 17, 413–433, doi:10.1002/we.1584, 2013.

Stull, R. B.: An Introduction to Boundary Layer Meteorology, Springer Science & Business Media, Dordrecht, the Netherlands, 670 pp., 1988.

Wagner, R., Courtney, M., Gottschall, J., and Lindelöw-Marsden, P.: Accounting for the speed shear in wind turbine power performance measurement, Wind Energy, 14, 993–1004, doi:10.1002/we.509, 2011.

Wang, H., Barthelmie, R. J., Clifton, A., and Pryor, S. C.: Wind measurements from arc scans with Doppler wind lidar, J. Atmos. Ocean. Tech., 11, 2024–2040, doi:10.1175/JTECH-D-14-00059.1, 2015.

Wyngaard, J. C.: Turbulence in the Atmosphere, Cambridge University Press, Cambridge, UK, 406 pp., 2010.